Acta Crystallographica Section B
Structural Science, Crystal Engineering and Materials
ISSN 2052-5206

In-situ laser synthesis of Nd–Al–O coatings: the role of sublattice cations in eutectic formation

Isabel de Francisco,[a] Jose Antonio Bea,[b] Angel Vegas,[c]* Juan Bautista Carda[d] and German Francisco de la Fuente[a]*

[a]Instituto de Ciencia de Materiales de Aragón (CSIC – University of Zaragoza), E-50018 Zaragoza, Spain, [b]Group of Applied Modeling and Instrumentation (GIMA), Aragón Institute of Engineering Research (I3A), University of Zaragoza, Spain, [c]Universidad de Burgos, Hospital del Rey s/n, E-09001 Burgos, Spain, and [d]Departamento de Química Inorgànica y Orgànica, Universitat Jaume I, E-12071 Castellón de la Plana, Spain

Correspondence e-mail: diegas2002@gmail.com, german.delafuente.leis@csic.es

Received 25 November 2014
Accepted 15 January 2015

Neodymium aluminate coatings have been prepared *in-situ* by the laser zone melting (LZM) method, using a CO_2 SLAB-type laser emitting at 10.6 µm. Polycrystalline Al_2O_3 commercial plates have been used as substrates, and coatings were prepared from the corresponding mixtures of powdered neodymium and aluminium oxides as starting materials. Microstructure, studied by SEM and phase composition, studied by XRD, proved the *in-situ* formation of a $NdAlO_3$/$NdAl_{11}O_{18}$ eutectic. As a result, a well integrated composite coating was formed. Nanoindentation tests are consistent with excellent integration between coating and substrate. Structural similarities between the eutectic components within the coating, as well as between these and the substrate, are consistent with the crystallographic concepts proposed by Vegas (Ramos-Gallardo & Vegas, 1997), where cation subarrays play an important role governing metal oxide structures. These structure sublattices are suggested as the driving force behind eutectic oxide formation.

1. Introduction

The formation of $Al_2O_3/Y_3Al_5O_{12}$ and $Al_2O_3/GdAlO_3$ eutectics was explained in previous work (de Francisco *et al.*, 2011) on the basis of the structural compatibility of the cation-sublattices of the two phases involved. In the case of the $Al_2O_3/Y_3Al_5O_{12}$ eutectic mixture, the structural compatibility was justified by the existence of a binary compound of the formula YAl_2, with the structure of the cubic $MgCu_2$ Laves phases, and how parts of this Friauf–Laves phase topology also exist in the cubic γ-phase of alumina. The latter may be reformulated as $Al_{2.8}O_4$ to indicate that this phase is, in fact, a defect spinel structure with an Al-skeleton also of the $MgCu_2$-type.

The oxidation of the YAl_2 Laves phase, as reported elsewhere (Errandonea *et al.*, 2008), does not yield the hypothetical spinel YAl_2O_4; the garnet $Y_3Al_5O_{12}$ is formed instead. It has also been shown, however, that the Y_3Al_5 garnet sublattice can be derived from that of the cubic Laves phases, in such a way that a sort of continuity exists between the γ-Al_2O_3 ($Al_{2.8}O_4$) and the garnet $Y_3Al_5O_{12}$ structures. That is, the similarity between both aluminium subnets would be the reason for the structural compatibility, and hence for eutectic formation.

In order to emphasize the importance of cation–sublattices in eutectic microstructures, the process can be represented as

$$Y_3Al_6O_{12}\,(3 \times YAl_2O_4) \rightarrow Y_3Al_5O_{12} + Al$$

Alumina-perovskite ($Al_2O_3/GdAlO_3$) is the observed eutectic product within the Al_2O_3–Gd_2O_3 system. This behavior might be explained from the same Laves phase $GdAl_2$,

Table 1
Samples prepared by LZM.

Code and corresponding Nd-alumina mixture coating precursor composition. Ideal eutectic compositions are given for comparison.

Samples	Formal composition	Nd_2O_3 (mol%)	Al_2O_3 (mol%)
Nd_1	$NdAlO_3$	50	50
Nd_2	$Nd_3Al_5O_{12}$	37.5	62.5
$NdAlO_3/NdAl_{11}O_{18}$		20	80

which, by a gradual increase of the Gd content, could convert into a metastable CsCl-type structure. This transformation has been reported for the $NbCr_2$ Laves phase, which transforms into a metastable b.c.c. (body-centred cubic) phase. This last conversion opens the possibility of the formation of $LnAlO_3$ perovskite from the $LnAl_2$ Laves skeleton, not a surprise when considering that the cation array of perovskites is of CsCl-type.

In the present article, this innovative point of view is applied to account for the $NdAlO_3/NdAl_{11}O_{18}$ eutectic mixture. According to the concept explained by Vegas in previous work (Errandonea *et al.*, 2008; Martinez-Cruz *et al.*, 1994; Ramos-Gallardo & Vegas, 1997; Vegas & Jansen, 2002; Santamaría-Pérez & Vegas, 2003; Santamaría-Pérez *et al.*, 2005; Vegas & García-Baonza, 2007; Vegas, 2011), the preservation of the corresponding alloy structures in oxides affords an explanation for the phase relations observed in these experiments and may contribute to the advancement of the understanding of eutectic systems empirically identified in the corresponding phase diagram (Wu & Pelton, 1992).

The presence of aluminium oxide components in aluminate composites offers, in addition, an important advantage owing to their potential chemical compatibility with alumina and porcelain-type industrial ceramic products. It opens the possibility of obtaining coatings with good interface strength and adequate chemical purity.

Moreover, an '*in-situ*' laser zone melting synthesis method (de Francisco *et al.*, 2011; Larrea *et al.*, 2002; Mora *et al.*, 2004; Lennikov *et al.*, 2007) has been recently developed and has proven to be adequate for the preparation of high melting ceramic coatings. It consists of a CO_2 laser scanner combined with a continuous furnace as the external heating source (Estepa & de la Fuente, 2006; Lennikov *et al.*, 2007). This processing method enables the consolidation of coatings based on practically any chemically compatible oxide material on alumina substrates. This is particularly favorable when such coatings exhibit high boiling temperatures during melting. With this method, it is possible to produce an extensive number of high melting point (up to 3273 K) materials, enabling the study of phase relations under extreme conditions.

The objective of this work is thus twofold; on the one hand, to explore the structural phase relations within the coatings obtained, taking into account the corresponding phase diagrams. On the other hand, to advance on the development of a new protocol in coatings design using the concept advanced by Vegas.

2. Experimental

2.1. Precursor preparation

Precursor materials were prepared from commercial powders corresponding to the stoichiometric compositions of (Nd_1) $NdAlO_3$ perovskite and (Nd_2) $Nd_3Al_5O_{12}$ garnet (Table 1).

Precursor coatings were thus prepared from the pure oxides Al_2O_3 (Sigma Aldrich, 99.7%), Nd_2O_3 (Alfa Aesar, 99.9%). The starting powder materials were milled in a Retsch 2000 Ball Mill (model MM2000, Resch, Haan, Germany) using an alumina grinding component, with isopropyl alcohol (PANREAC, chemical purity) as a liquid suspension medium with a solid content ranging between 62 and 65 weight %. The resultant suspension was deposited onto commercial $8 \times 10 \times 1$ mm^3 polycrystalline alumina plates using the dip-coating method. The substrate was immersed into the suspension and extracted vertically at a speed of 10 mm s^{-1}. The coated plates were dried for a period of 48 h at room temperature before laser processing.

2.2. Laser zone melting (LZM)

The LZM process was carried out using a recently patented laser-furnace apparatus. A 350W Rofin–Sinar SLAB-type CO_2 laser emitting at a wavelength of $\lambda = 10.6$ μm is introduced into an electrically heated, continuous roller furnace manufactured by Nannetti. The laser beam is focused into the moving sample inside the furnace using a commercial galvanometer optical beam scanning system integrated into the laser optical path (Rofin). Such a system transforms the circular cross-section beam into a scanning line measuring 1 mm in thickness and a variable, predetermined width. The width was set to 40 mm for all of the samples reported here. The laser line focus was directed to the sample as shown in Fig. 1. The stage movement speed was respectively established at 1500 and 3000 mm h^{-1} for different experiments, but the laser power was fixed at 350 W in all cases. The resistance furnace

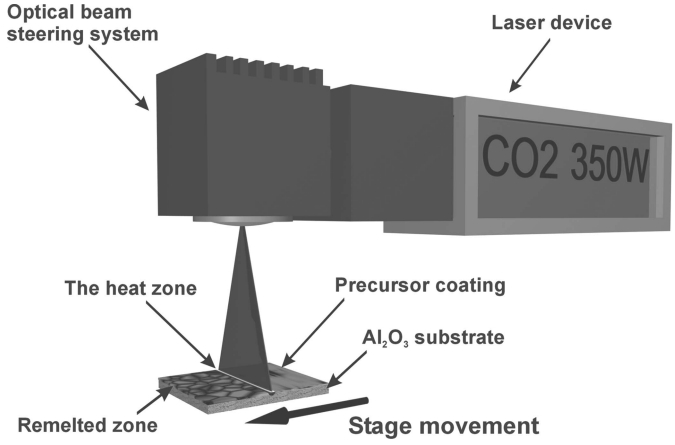

Figure 1
Laser zone melting apparatus used for this work. It includes a SLAB-type CO_2 laser resonator, an optical beam steering system that focuses the laser beam onto a line at the coated substrate surface. The substrate is moved at a constant rate in an orthogonal direction to the laser line.

temperature was fixed for each sample within a range between 973 and 1573 K, in order to avoid the appearance of cracks in the laser-treated products.

2.3. Characterization

Sample microstructure was studied using a Jeol 6400 scanning electron microscope, observing polished longitudinal and transversal cross-sections (with respect to the sample solidification front movement direction), as well as the surface of as-processed samples. Elemental analyses were performed during SEM observation using a coupled Oxford Instruments EDS unit. The crystalline phases of the samples were studied by X-ray diffraction using a D-Max Rigaku diffractometer (Cu $K\alpha$) with a rotating anode.

Nanoindentation tests were performed with a Nano Indenter G200 (Agilent Technologies Inc.) on polished longitudinal cross-section samples (parallel to the solidification direction). Arrays of 100 indentations were marked for each characterized sample within a 25 × 4 matrix, using a 20 μm spacing between indentations. Each indentation array was started at the surface of the coating and ended deep into the substrate, in order to study the mechanical behavior of samples along their cross section and identify potential heat-affected zones (HAZ), as well as features related to microstructure and phase composition. The tests were carried out using a trigonal Berkovich indenter and fused silica for standard area-function calibration, maintaining a constant drift rate of 0.05 s^{-1} and a 2000 nm depth limit.

3. Results and discussion

3.1. XRD characterization

In general, for rare-earth (RE) aluminate synthesis, competition between perovskite and garnet phases is a key question. In the case of neodymium aluminates, the two competitor phases are perovskite ($NdAlO_3$) and the hypothetical $Nd_3Al_5O_{12}$ garnet phase. Klimm *et al.* (2007) suggested that the garnet phase is stable below 1200 K, decomposing at higher temperatures to $NdAlO_3$ and α-Al_2O_3. They also pointed out that even if the Nd-garnet does not appear in the Nd_2O_3-Al_2O_3 phase diagram, it might exist as a metastable phase. Nevertheless, the decomposition into $NdAlO_3$ and α-Al_2O_3 could explain why the Nd-garnet does not appear in the eutectic composition and instead the $NdAlO_3$ perovskite is present.

According to the X-ray diffraction measurements obtained from the surface of samples corresponding to the two different starting mixtures, Nd_1 and Nd_2, the same crystalline component phases were obtained in the corresponding resultant laser-treated products.

Mixtures Nd_1 and Nd_2 correspond to the stochiometric composition of the perovskite-type neodymium aluminate and the neodymium garnet, respectively. Regardless of the precursor composition, three different phases were obtained in the laser product: Corundum (α-Al_2O_3), perosvkite-type neodymium aluminate ($NdAlO_3$) and a neodymium hexaaluminate ($NdAl_{11}O_{18}$), as confirmed by diffraction patterns obtained on Nd_1 and Nd_2 samples (Fig. 2).

For both mixtures Nd_1 and Nd_2, the complete formation of the observed product phases should have been disfavored due to insufficient alumina content, in agreement with traditional ceramic synthesis. In the latter, diffusion processes dominate the associated solid state reactions and the substrate material should react only to a limited zone, reducing its role in phase formation. Taking advantage of the laser zone melting method, however, the reaction zone is melted, allowing the substrate to play a relevant role in the process. In this manner, excess Al_2O_3 incorporates into the molten zone and enhances formation of corundum and neodymium hexaaluminate phases.

3.2. SEM characterization

Surface and cross-section polished CO_2 laser-treated precursor-coated samples were observed by scanning electron microscopy; measured coating thicknesses exhibited values ranging between 130 and 250 μm. In addition, the presence of a binary $NdAlO_3$/$NdAl_{11}O_{18}$ eutectic was revealed within the coating as confirmed by EDX analyses. This was obtained from precursor compositions Nd_1 and Nd_2 and it consists of an interpenetrating network of two phases. These are composed of $NdAlO_3$ fibers (light gray contrast) imbedded within a ß-alumina type $NdAl_{11}O_{18}$ matrix (dark gray contrast) (Iyi *et al.*, 1984; Mizuno *et al.*, 1977).

The Al_2O_3 excess, apparently introduced by convection currents during the laser treatment (Larrea *et al.*, 2002; Lennikov *et al.*, 2007), has been deposited as faceted zones in samples Nd_1 and Nd_2. This extra alumina contribution modifies the effect expected from the original starting composition within the precursor coatings on the obtained microstructure.

Table 1 shows that both Nd_1 and Nd_2 starting precursors are deficient in Al_2O_3 compared with the ideal eutectic composition (Mizuno *et al.*, 1977; Coutures, 1985; Klimm *et al.*, 2007).

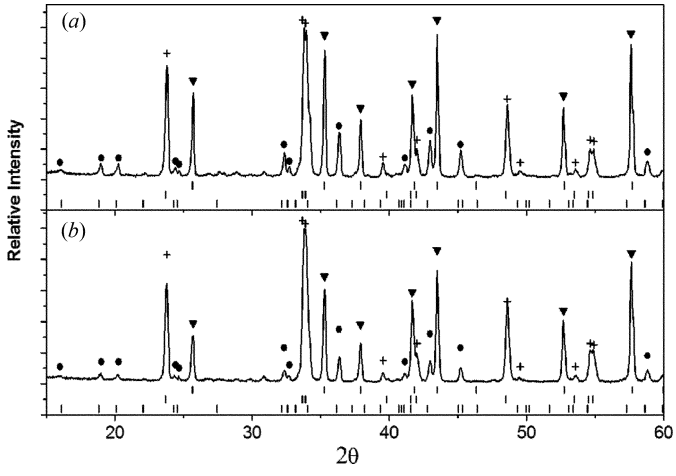

Figure 2
XRD spectra of samples obtained by LZM using nominal compositions (*a*) Nd_1 ($NdAlO_3$) and (*b*) Nd_2 ($Nd_3Al_5O_{12}$). Circles: $NdAl_{11}O_{18}$ phase; plus signs: $Nd_3Al_5O_{12}$ phase; filled triangles: Al_2O_3 phase.

Convection within the molten coating during laser treatment induces partial melting, followed by an uptake of substrate material, thereby generating an enrichment of alumina that explains the growth of the observed eutectic. This alumina enrichment also permits the recrystallization of faceted phases in both types of samples.

Fig. 3 shows sample types Nd_1 and Nd_2 grown with a stage movement speed of 1500 mm h^{-1} ($Nd_1$1500 and $Nd_2$1500). They present faceted α-Al_2O_3 grains (black contrast). Fig. 4(*a*) shows the Nd_1 sample type grown with a stage movement speed of 3000 mm h^{-1} (Nd_1 3000). Two different zones may be observed: One with facetted α-alumina (black contrast) and another one with facetted neodymium hexaaluminate (dark gray contrast). In this case, the composition of the phase that solidifies in facetted zones during cooling is either α-alumina or neodymium hexaaluminate, depending on the concentration of alumina in the melt. During the process, the latter varies as a function of time as the system tends to achieve

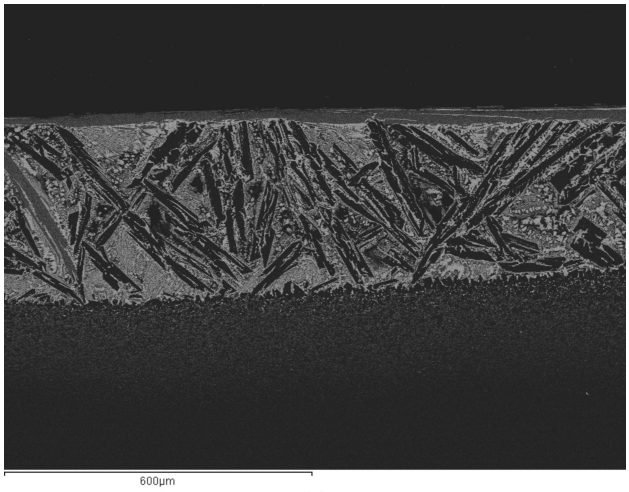

(*a*)

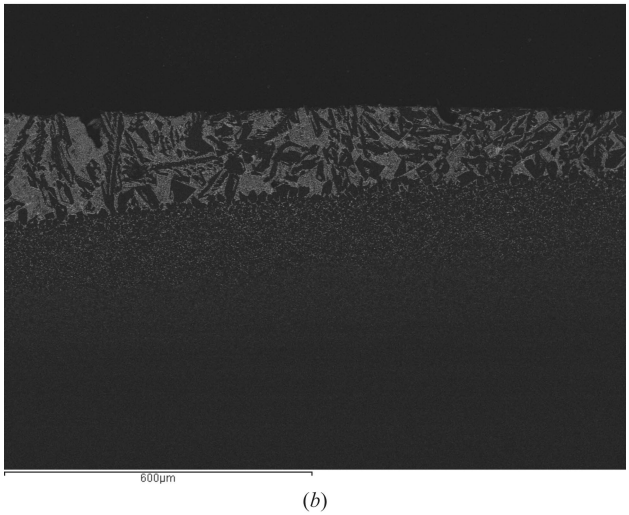

(*b*)

Figure 3
Secondary electron micrograph of the LMZ coatings grown with a stage movement speed of 1500 mm h^{-1}. (*a*) Sample Nd_1 ($NdAlO_3$); (*b*) sample Nd_2 ($Nd_3Al_5O_{12}$).

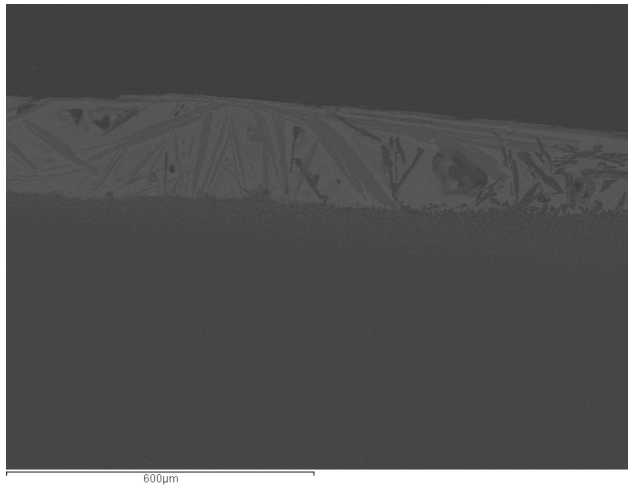

(*a*)

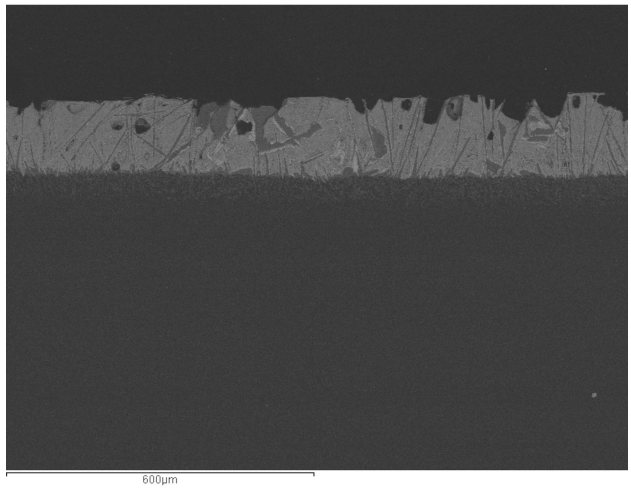

(*b*)

Figure 4
Secondary electron micrograph of the LMZ coatings grown with a stage movement speed of 3000 mm h^{-1}. (*a*) Sample Nd_1 ($NdAlO_3$); (*b*) sample Nd_2 ($Nd_3Al_5O_{12}$).

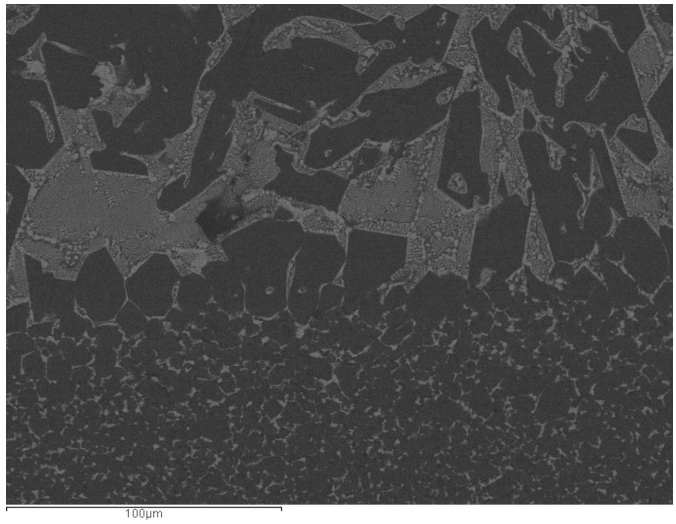

Figure 5
Secondary electron micrograph of the interface between the LMZ coating and the Al_2O_3 substrate of the sample Nd_2 grown at 1500 mm h^{-1}.

Table 2
Samples prepared by LMZ.

Profile of the elemental analysis for Nd along the coating–substrate interface, as exemplified in Fig. 6, for sample Nd_1.

Spectrum No.	Nd ($NdAl_{11}O_{18}$) (Nd atomic %)	Spectrum No.	Nd($NdAlO_3$) (Nd atomic %)
1	2.76	9	1.86
2	0.92	10	1.00
3	–	11	1.16
4	–	12	0.82
5	–	13	0.80
6	–	14	–
7	–	15	–
8	–	16	–

equilibrium. Consequently, the composition of the facetted zones also varies accordingly.

In sample type Nd_2 3000 (Fig. 4*b*), however, the composition of the faceted zone keeps constant as neodymium hexaaluminate. According to this observation, the composition of the faceted zones depends mainly on the solidification rate, but also to some extent on the starting composition of the samples.

Fig. 5 shows that the obtained coatings are free of cracks at the coating–surface interface. This interface contains a segregation of faceted α-Al_2O_3 and neodymium hexaaluminate coupled to the $NdAlO_3$ phase, whithin the grain junctions near the coating. A transition zone is furthermore observed to contain the original alumina grains from the substrate, separated within their intergranular spaces by a layer of compounds stemming from the coating. In the zone with faceted α-alumina of sample Nd_1, the compound that diffuses into the substrate is $NdAlO_3$. In contrast, the zone containing faceted neodymium hexaaluminate appears as a consequence of $NdAl_{11}O_{18}$ diffusion. This compound diffusion is found to conform, with the substrate, a new multiphase adjusting layer.

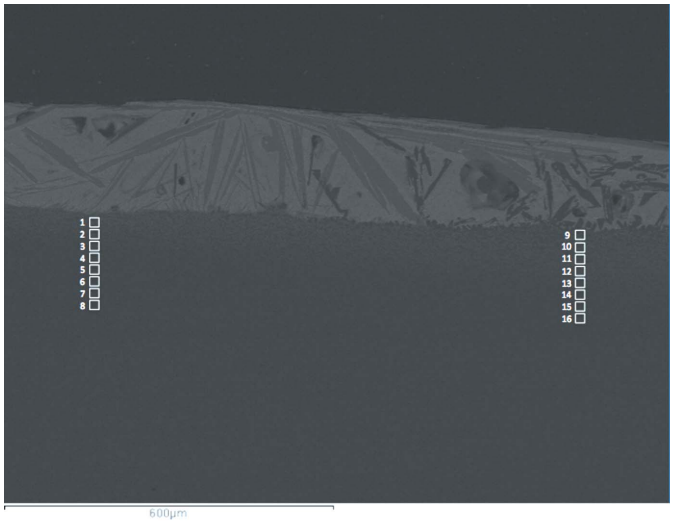

Figure 6
Elemental microanalysis areas taken on sample Nd_1 ($NdAlO_3$) grown at 3000 mm h^{-1} throughout the coating–substrate interface.

Fig. 6 and Table 2 show the differences in composition across the coating–substrate interface as determined by EDS, in the two different zones, with faceted α-alumina and faceted neodymium hexaaluminate. Fig. 6 shows the elemental microanalysis areas taken on sample Nd_1 in both zones across the coating–substrate interface. Table 2 shows the downward diffusion across the interface of the corresponding coating compound. The thickness of the multilayer varies depending on the diffusing compound. It appears approximately as 150 µm for $NdAlO_3$ and 50 µm for Nd hexaaluminate diffusing compounds.

3.3. Mechanical properties: nanoindentation

Nanoindentation tests were performed in order to ascertain the elasto-plastic response of each component phase of the eutectic. The indentation arrays were performed on the coating, on the transition zone between coating and substrate and the affected substrate, in order to characterize each unique sample zone (Fig. 7). In studied samples, the coating

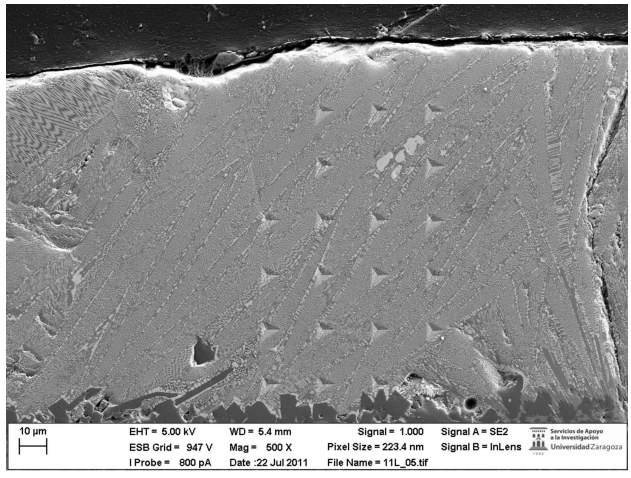

(*a*)

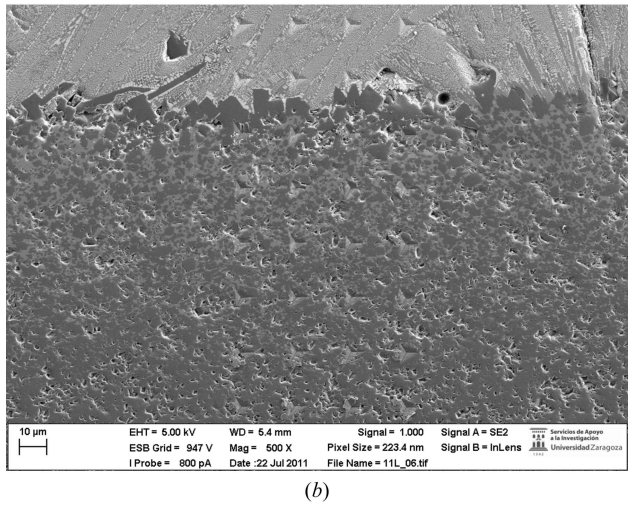

(*b*)

Figure 7
Secondary electron micrographs of the indentation arrays include: (*a*) the coating, (*b*) the transition zone between coating and substrate, and the affected substrate of the Nd_1 sample grown at 3000 mm h^{-1}.

hardness is found to be around 20 GPa, very similar to that of the polycrystalline alumina. This can be explained by the high alumina content of the eutectic coating, as well as for its crystallographic structure similarity described below.

The coatings are formed by cells of the binary eutectic $NdAlO_3/NdAl_{11}O_{18}$, on one hand, and by faceted α-Al_2O_3 or neodymium hexaaluminate phases, on the other. Samples were prepared at two different stage movement speeds, 1500 and 3000 mm h^{-1} (Fig. 8). Depending on this condition, the α-Al_2O_3 or neodymium hexaaluminate phase grains may be larger than the indentation feature. Thus, the indentation may take place on faceted α-Al_2O_3 or neodymium hexaaluminate grains.

If the eutectic hardness is different from that of α-Al_2O_3 or $NdAl_{11}O_{18}$, the indenter could drag the non-eutectic zone downwards. The hardness data could thus be controlled by faceted α-Al_2O_3 or neodymium hexaaluminate phases, introducing some scattering in the obtained data, mainly in the zone of the sample corresponding to the coating and transition layers. Samples obtained at 3000 mm h^{-1} present less scattering than those treated at 1500 mm h^{-1} (Fig. 9). In samples treated at 3000 mm h^{-1}, α-Al_2O_3 or $NdAl_{11}O_{18}$ grains are smaller than those treated at 1500 mm h^{-1}.

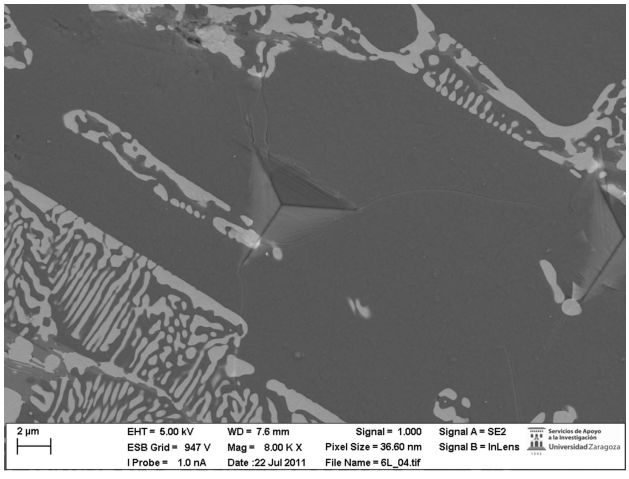

(*a*)

(*b*)

Figure 8
Secondary electron micrograph of the indentation area of sample Nd_2 (*a*) grown at 1500 mm h^{-1} and (*b*) grown at 3000 mm h^{-1}.

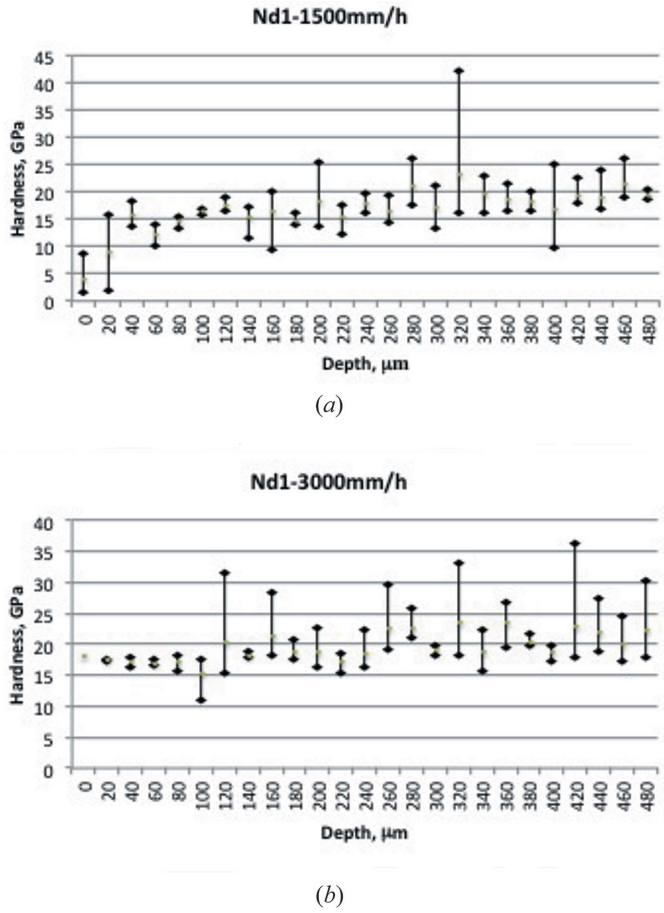

(*a*)

(*b*)

Figure 9
Variation of the nanoindentation hardness as a function of sample depth for (*a*) sample Nd_1 grown at 1500 mm h^{-1} and (*b*) sample Nd_2 grown at 3000 mm h^{-1}.

3.3.1. Mechanical behavior and microstructure: a computational approach. The aim of this section is to clarify the results observed for the indentation of the complex eutectic system studied here. Consequently, assuming the same linear elastic behavior for the two different phases present in the eutectic, it is necessary that they exhibit the same plastic behavior in order to get the same permanent deformation

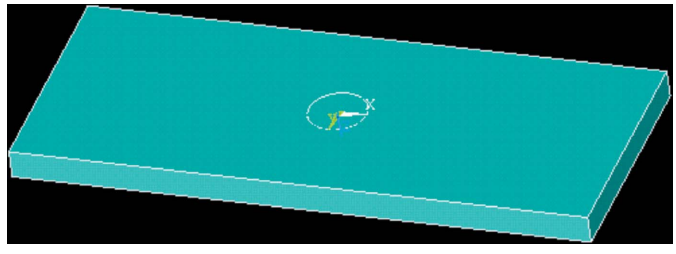

Figure 10
Geometry and boundary conditions. On the bottom, only vertical displacements are zero. The thickness, width and height are 5, 100 and 40 mm, respectively. The central circle has a diameter of 10 mm.

under identical loading conditions (uniform pressure). Furthermore, the main idea is to simulate a simplified 'nano-indentation test' applying pressure instead of a nano-indenter. This is to avoid the nonlinearities that appear in every contact problem solved with FEMs, which causes scattering of the displacement, strain and stress fields that solve the problem.

The simulated geometry is shown in Fig. 10. In all cases, the applied pressure was fixed at 800 MPa. The phase behavior used in all the simulations is based on bilinear isotropic work hardening. That means that only two parameters control the plasticity: the yield stress and the tangent modulus.

For every simulation, two load steps have been used: an initial ramp from 0 to 800 MPa, and a second load step to decrease the pressure until it vanishes. The simulation was carried out with *ANSYS* Version 14.5 software, using hexahedral element type SOLID185, defined by eight nodes having three degrees of freedom at each node. These include translations in the nodal x, y and z directions. Each element may account for plasticity, large deflection and large strain capabilities, among other features. The model includes 47 280 elements.

The mesh used in all the simulations for this geometry is shown in Fig. 11(a), and the boundary conditions in Fig. 11(b), where the blue symbols mean zero displacement perpendicular to the surface, and the red arrows represent the applied pressure. This is a quarter model obtained from applying symmetry conditions. The whole problem is shown in Fig. 11(b).

For the first simulation, a yield stress of 146 MPa and a tangent modulus of 1380 MPa are used. The displacement field obtained after force removal is shown in Fig. 12. The finite element method gives the vector displacement field (ux, uy, uz) for the whole solid, meaning that every single point of the solid, with initial Cartesian coordinates X, Y, Z, moves to new positions $X + ux$, $Y + uy$, $Z + uz$ due to the mechanical conditions applied. The maximum absolute value for the displacement field uz is 0.769727 mm, and the maximum value is 0.058211 mm. The deformed shape is also shown in this

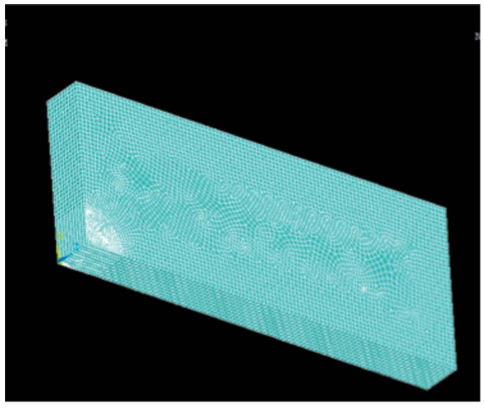

(a)

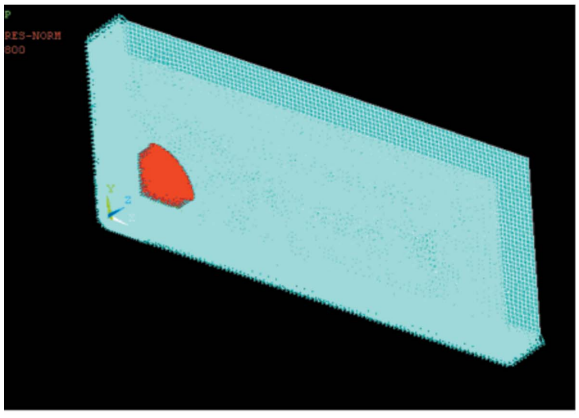

(b)

Figure 11
Hexahedral elements mesh (a) and boundary conditions (b).

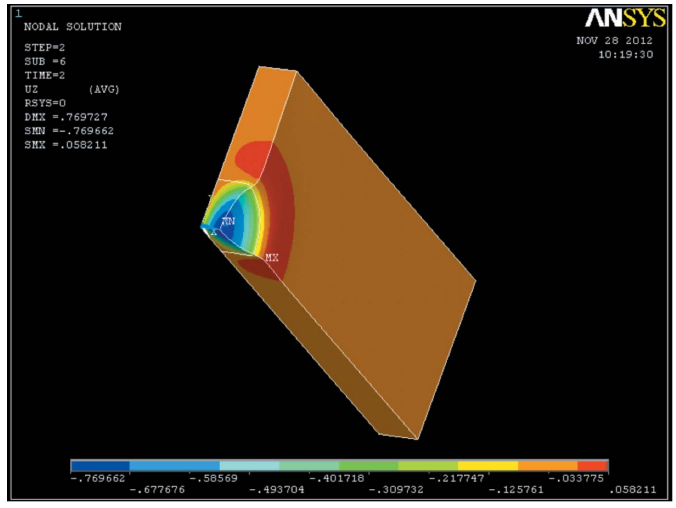

Figure 12
Permanent displacement field after pressure removal.

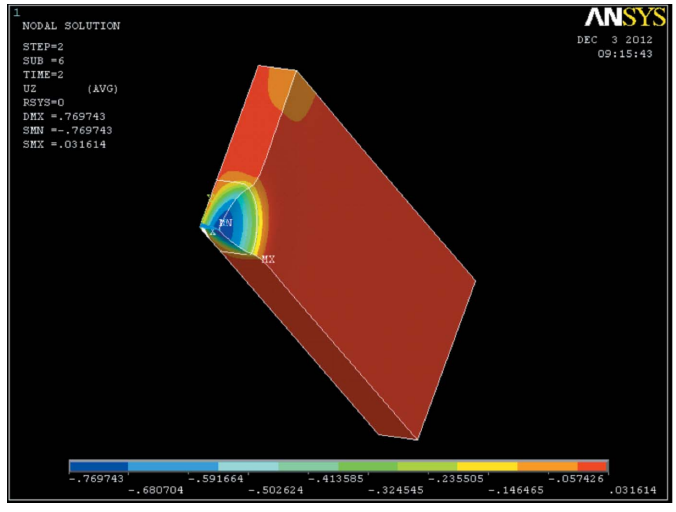

Figure 13
Permanent displacement field after pressure removal, for a tangent modulus of 2101.7 MPa.

Table 3
Some examples of the structures formed by cations in oxides compared with the structures of the alloys themselves.

The data show the pressure effects exerted by the O atoms as well as the inverse transitions occurring by heating due to the compensation of pressure with temperature.

Element/alloy *Structure type*	Oxide	Cation substructure	HT-phase HP-phase	Cation substructure
Si	SiO_2	HP-ZnTe	HT-SiO_2	Si
Si	Quartz	HgS-cinnabar	Cristobalite	
BaS	[BaS]O_4	FeB	HT-cubic	NaCl
NaCl	Barite		[BaS]O_4	
Y_5Si_3	$Y_5Si_3O_{12}N$	Mn_5Si_3	–	–
Mn_5Si_3				
Ca_5As_3	$Ca_5(AsO_4)_3Cl$	Mn_5Si_3	–	–
Mn_5Si_3				
Ca_5P_3	$Ca_5(PO_4)_3F$	Mn_5Si_3	–	–
Unknown	Apatite			
KCl	[KCl]O_3	CrB (*B*33)	HT-$KClO_3$	NaCl-blocks
NaCl, CsCl(HP)			HP-$KClO_3$	CsCl-distorted
BaGe	[BaGe]O_3	CrB	HP-$BaGeO_3$	CsCl
CrB			perovskite	
BaSn	[BaSn]O_3	CsCl	–	–
CrB, CsCl				
SrSe	[SrSe]O_4	Monazite	–	–
NaCl		(RE)PO_4		
Li_2S	**[Li_2S]**O_4 distorted	CaF_2	HT-Li_2SO_4	Cubic CaF_2
CaF_2, $PbCl_2$	phenakite	Very distorted		
Cs_3Bi	[Cs_3Bi]O_3	Fe_3Al distorted	–	–
BiF_3, Fe_3Al				
K_2S_2	[K_2S_2]O_6	NiAs	–	–
NiAs				
Na_2S	[Na_2S]O_4 thenardite	$TiSi_2$	HT-Na_2SO_4	Ni_2In
CaF_2, $PbCl_2$, Ni_2In		THE-Rb_2S		
Ag_2S	[Ag_2S]O_3	$PbCl_2$	–	–
$PbCl_2$				
Ni_2Si	[Ni_2Si]O_4 olivine	Ni_2In	–	–
Co_2Si, Ni_2In				

figure, and the colors of the picture describe the permanent displacement field due to the plastification process.

Now the idea is to use a different yield stress, *i.e.* 140 MPa, in order to answer the following question: What is the tangent modulus that causes the same maximum absolute value, keeping constant the Young modulus, the geometry and the applied pressure? The answer to this question may be obtained by making use of a parametric file as an input for *ANSYS*, in which the Newton–Raphson algorithm is implemented (the derivatives are approximated by finite differences). Depending on the desired precision, a solution (tangent modulus of 2101.7 MPa, maximum absolute value for *uz* 0.769743) is shown in Fig. 13. In Fig. 14 it is drawn at a higher resolution (tangent modulus of 2101.77 MPa; maximum absolute value *uz* of 0.769727).

Comparing the results with those shown in Fig. 12, the whole permanent displacement field for *uz* is not constant, in spite of the fact that the maximum absolute value for *uz* is the same. The conclusion is that it is not possible to obtain the same permanent displacement field for two distinct phases or solids having the same Young modulus and different tangent modulus, even in the case when both tangent moduli cause the same maximum absolute value for the permanent displacement *uz*, applying the same force in both cases (pressure). Reference to this conclusion will be made in the following discussion, in order to ascertain the structural relationship intrinsic to eutectic formation.

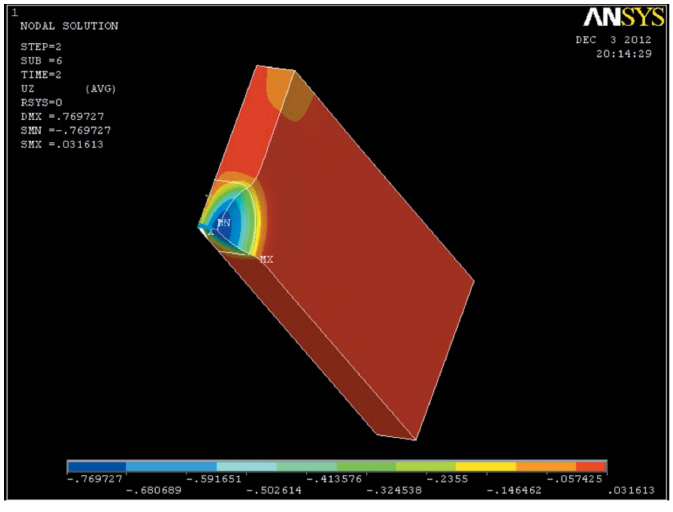

Figure 14
Permanent displacement field after pressure removal (tangent modulus 2101.77361 MPa).

4. Structural relationships and eutectic phase formation

In previous work (de Francisco *et al.*, 2011) a novel approach towards furthering our understanding of eutectic formation was proposed that is based on the model developed by Vegas & co-workers. This model contemplates the cation–sublattices of the phases involved in the eutectic as responsible for eutectic component coupling at the atomic level. As reported by de Francisco *et al.* (2011), the rare earth element used plays an important role in the final product obtained. It should be recalled that in the yttria-containing compounds (de Francisco *et al.*, 2011) the eutectic is formed by the perovskite/garnet pair, whereas the $NdAlO_3/NdAl_{11}O_{18}$ pair conforms to the present eutectic mixture.

4.1. New approach to describe oxide structures

The concept developed by Vegas and co-workers to increase our understanding of crystal structures is an exten-

sion of the new approach proposed by O'Keeffe & Hyde (1985). They realised that, in most of the structure types, the cation sub-arrays adopted the structures of elements or simple alloys, a feature that led them to consider oxides as 'oxygen-stuffed alloys'. In some cases, like in β-Ca_2SiO_4, the Ca_2Si sub-structure (of the $PbCl_2$-type) corresponded with that of the Ca_2Si alloy itself and the same occurs in the $Y_5Si_3O_{12}N/Y_5Si_3$ pair (see Table 3). However, in most of the examples reported (O'Keeffe & Hyde, 1985), the cation sub-array differed from that of the alloy. Thus, the Ca_5P_3 partial structure in apatite $[Ca_5(PO_4)_3(OH)]$ has not been synthesized so far and the BaS subarray (FeB type) in $BaSO_4$ (barite) does not correspond to the rocksalt structure of BaS. The lack of a universal behavior led Vegas and co-workers to intensively explore the reasons for that discrepancy, trying to find out a general approach accounting for most of the similarities/discrepancies observed in the alloys/oxides pairs.

As will be shown below, the concept developed by Vegas and co-workers (Martinez-Cruz *et al.*, 1994; Ramos-Gallardo & Vegas, 1997; Vegas, 2000; Vegas & Jansen, 2002; Santamaría-Pérez & Vegas, 2003; Santamaría-Pérez *et al.*, 2005; Vegas & García-Baonza, 2007; Errandonea *et al.*, 2008; Vegas, 2011) has demonstrated that the preservation of the structure of the elements/alloy in their corresponding binary/ternary/quaternary oxides is more general than it was believed. Reports published by Blatov and co-workers, concerning the topological comparison of the tetrahedral structures $M_y(TO_4)_z$ with those of the binary compounds A_yX_z (Ilyushin *et al.*, 2004), the analysis of the borates, carbonates and nitrates (Blatov & Zakutkin, 2002) and the crystallochemical analysis of binary compounds and simple salts $M_y(LO_3)_z$ (L = S, Se, Te, Cl, Br, I; Blatov & Peskov, 2006) all deserve to be considered in this context.

Overall, this new insight has provided a rational explanation for many oxide structures, as well as for many phase transitions and, hence, for the structural relationships observed among the above eutectic phases (de Francisco *et al.*, 2011). In the present work, this innovative point of view is applied to the $NdAlO_3/NdAl_{11}O_{18}$ eutectic mixture, in order to test its validity with the measurement of a physical parameter.

4.2. The principles of the new approach

For readers that are not familiar with these new viewpoints, we will try to summarize using a few fundamental principles:

(i) The oxidation of an element/alloy is equivalent to the application of pressure (Martinez-Cruz *et al.*, 1994). This principle was discovered after the high-pressure experiments carried out on the BaSn alloy (Beck & Lederer, 1993). At 3.5 GPa the BaSn alloy undergoes the transition CrB (B33) → CsCl (B2), the latter corresponding to the BaSn subarray of the $BaSnO_3$ perovskite. Both compounds BaSn and $BaSnO_3$ have not only the same skeleton but also the same unit-cell dimensions (4.07 and 4.11 Å, respectively). This coincidence led Martinez-Cruz *et al.* (1994) to speculate about the existence of the equivalence between oxidation and pressure, an idea illustrated with the diagrams of Fig. 15.

(ii) If cations stabilize the structure of high-pressure phases of the corresponding alloy in the oxide, then the opposite conversion should also be possible, *i.e.* by heating the oxide, the alloy structure, stable at ambient pressure, can be recovered. The ZnS (blende)/$ZnSO_4$ pair, represented in Fig. 16, illustrates this behavior: the zinc blende structure of ZnS is lost in the oxide $ZnSO_4$ (zincosite) ($CuSO_4$-type; Kokkoros &

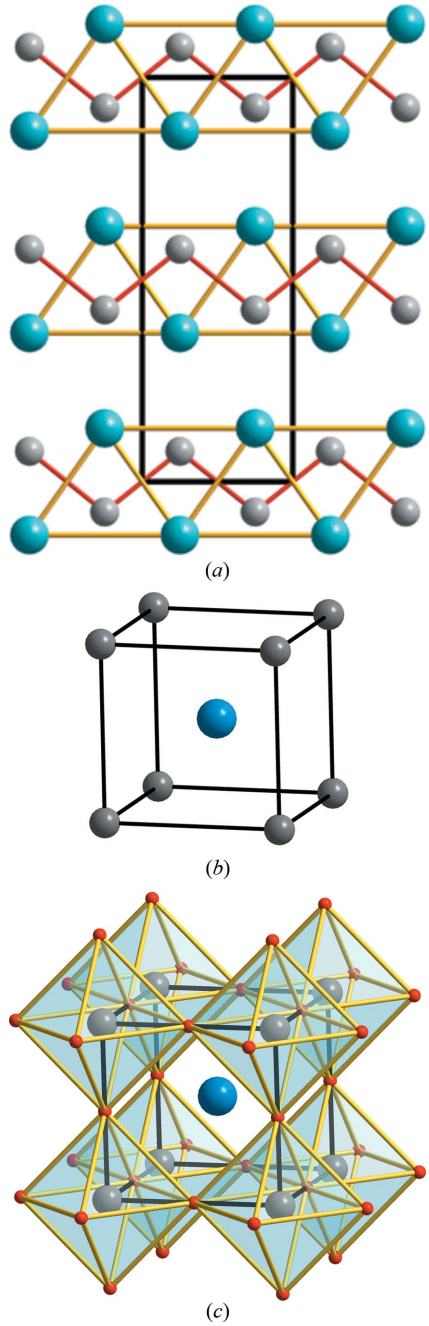

Figure 15
Scheme showing the equivalence between oxidation and pressure. (*a*) The ambient pressure structure (*B*33) of the BaSn alloy (*Cmcm*). (*b*) The *B*2 structure of the same alloy at 3.5 GPa. (*c*) The perovskite structure of $BaSnO_3$ (*Pm*3*m*) showing that its BaSn sub-array is identical to the HP-phase of the alloy in (*b*). The SnO_6 octahedra are drawn as solid transparent polyhedra. Ba: blue; Sn: grey; O: red.

Rentzeperis, 1958). As shown in Fig. 16(*b*), oxidation transforms the blende [ZnS]-subarray into a NiAs-type structure.

However, as expected, the process reverts by heating (see Fig. 16*c*). At high temperature (973 K), $ZnSO_4$ transforms to a cubic phase with the high-cristobalite structure (Spiess & Gruehn, 1979) in which the [ZnS]-subarray recovers the blende structure. This is an example of recovering the ambient pressure phase when pressure is compensated by heating. Many other examples of this behavior were reported in the article of Vegas & Jansen (2002).

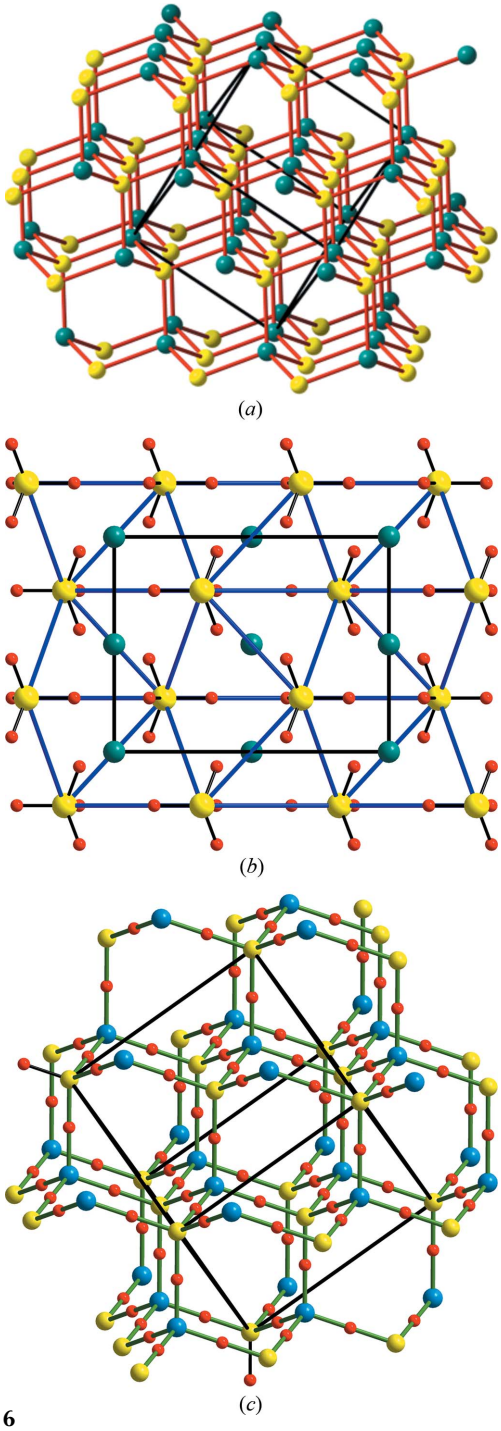

Figure 16
Scheme showing the effect of the pressure exerted by the O atoms when inserted into the network of an elemental structure or alloy as well as the opposite effect of temperature. (*a*) The diamond-related structure of zinc blende (ZnS). (*b*) The structure of $ZnSO_4$ formed by an h.c.p. [hexagonal close packed?] array of S atoms with all octahedra filled by the Zn atoms. (*c*) The structure of the high temperature phase of $ZnSO_4$ in which the original skeleton of the zinc blende (*a*) has been recovered in the form of a cristobalite-related structure. Zn: blue; S: yellow; O: red.

(iii) In some oxides, the cation subarrays do not fit to any alloy structure. In these cases, they can be regarded either as strong distortions of elemental structures or to intermediate states between the two structures involved in a phase transition. This is the case for the olivine Fe_2SiO_4, whose Fe_2Si-subarray (Ni_2In-type) is close to the structure of the high-temperature phase of Fe_2Si. In the latter, the structure was determined on a sample quenched at very high temperature. Its structure is a distortion of the regular Ni_2In-type structure of the oxide, but it shows distortion that indicates that the alloy had not yet reached the regular structure.

For these reasons, it has been suggested elsewhere (Vegas, 2000) that the validity of the concept of 'real stuffed alloys' could be extended considerably and thus generalized, if the cation arrays, in oxides, are regarded as *metastable structures of the corresponding alloy*.

(iv) The above assertion can be applied to those cases in which the elemental structure appears distorted or fragmented

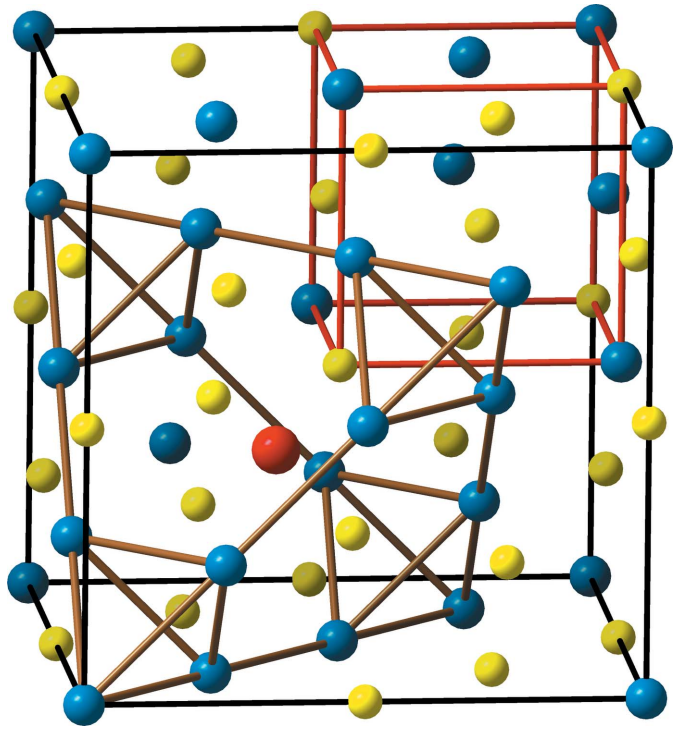

Figure 17
Drawing containing the eight unit cells of f.c.c.-Al. The array has been divided into two identical and complementary sets colored as blue and yellow spheres. Each one corresponds to the Al-subarray in spinel ($MgAl_2O_4$) and in the analog γ-Al_2O_3. In the blue moiety some Al—Al bonds have been connected with brown lines to outline the network of Al_4 tetrahedra as well as the truncated tetrahedron centered by a red sphere representing the Mg atoms in spinel or the Al atoms in γ-Al_2O_3. In the upper right side of the drawing one unit cell of f.c.c.-Al has been remarked with red lines.

in pieces that nevertheless preserve structural features of the parent element. Thus, in corundum α-Al_2O_3, the Al-subarray does not correspond to any elemental structure but it can be thought of as derived from an opening-up of the f.c.c.-Al [face-centered cubic] structure. On the contrary, in β- and γ-Al_2O_3 the Al-subarrays contain infinite fragments of f.c.c.-Al as can be seen in Fig. 17.

However, these discrepancies become less controversial when compared with oxides of other elements of the same Group 13. For example, the cubic structure of C-In_2O_3 (bixbyite-type) preserves, with small distortions, the tetragonal structure of In (*I*4/*mmm*) (Ramos-Gallardo & Vegas, 1995), but in extreme conditions (ball milling method) In_2O_3 yields the corundum-type structure. This issue is important because if both structures (corundum and bixbyite) are possible with In, they can also occur in Ga- and Al-oxides. Having this in mind, the cation substructure in corundum might well be seen as a metastable structure of Al (Ramos-Gallardo & Vegas, 1996), stabilized by the effect of the O pressure.

4.3. Some examples illustrating the new approach

The above assertions are illustrated with the examples collected in Table 3. In some cases (Y_5Si_3, Ca_5As_3, BaGe, Cs_3Bi, K_2S_2, Ag_2S and Ni_2Si) the structure of the alloy (column 1) is preserved in the oxide (column 2). Only in some cases, the oxide distorts to some extent the ideal structure.

In other cases (Si, BaS, KCl and Ca_5P_3) oxidation produces an effect strong enough that HP phases of the element/alloy stabilize in the oxides. Thus, silicon yields quartz in which the Si structure is similar to the cinnabar (HgS) structure or to the HP-ZnTe that is an intermediate phase in the transitions sequence: blende/wurtzite $\rightarrow$ cinnabar $\rightarrow$ NaCl. Now it is easy to understand why, by heating, quartz transforms into cristobalite recovering the Si structure (see Table 3).

In BaS, oxidation forms the barite structure whose BaS subarray is of the FeB-type. This feature is consistent with the fact that the FeB structure can be an intermediate in the sequence NaCl $\rightarrow$ CrB/FeB $\rightarrow$ CsCl. Thus, oxidation of the NaCl structure yields the formation of the HP-FeB structure. When the latter is heated, the NaCl array is recovered in the HT-$BaSO_4$ (see Table 3).

In KCl (NaCl at room pressure) the oxidation yields the formation of $KClO_3$, with a KCl-substructure of the CrB-type. Similar to BaS, the CrB structure is intermediate in the transitions path NaCl $\rightarrow$ CrB $\rightarrow$ CsCl and this explains the stabilization of the HP-CrB structure in $KClO_3$. The important outcome here is that, under pressure, $KClO_3$ transforms into a CsCl-type structure that is rhombohedrally distorted (angle α = 85°). This example shows another important conclusion: *cations undergo their own transitions in spite of forming part of an oxide*.

The situation differs in apatite $Ca_5(PO_4)_3F$. The Ca_5P_3 phosphide has not been reported so far. Its appearance in apatite means that it might be a metastable phase stabilized by the pressure exerted by the O atoms and, hence, it should be a firm candidate to be obtained at HP. This prediction is supported by the fact that Ca_5As_3 does exist with the same Mn_5Si_3-type structure (see Table 3) and agrees with the general trend followed within a group, *i.e.* the structures adopted by heavier elements are obtained at HP for the lighter ones.

Finally, Na_2S also offers important features. It is anti-fluorite at ambient pressure and undergoes the transitions $CaF_2 \rightarrow PbCl_2 \rightarrow Ni_2In$ by increasing pressure (Vegas, 2011). In Na_2SO_4 (thenardite) the [Na_2S]-subarray has the $TiSi_2$-type structure (*Fddd*). However, by increasing temperature, Na_2SO_4 (thenardite) undergoes the transitions *Fddd* $\rightarrow$ *Cmcm* $\rightarrow$ *Pnma* $\rightarrow$ $P6_3/mmc$, the latter recovering the Ni_2In structure of the second HP-phase of Na_2S (Vegas & García-Baonza, 2007; Vegas, 2011). It is important to outline that the $TiSi_2$-type structure, stabilized in the sulfate (thenardite), has never been observed in any alkali sulfide. Although this structure-type was theoretically predicted for the analog Rb_2S (Schön *et al.*, 2004; see Table 3), these authors failed to recognize its similarity with the [Na_2S]-subarray of Na_2SO_4 (thenardite). A study of which has since been made by Vegas & García-Baonza (2007) and more recently analyzed by Vegas (2011).

5. The structures involved in the eutectics

5.1. The alloys

To illustrate to the reader, we would like to start by describing the Nd–Al phases that are closely related to the cation arrays of the ternary oxides. The 1:1 alloy contains two phases: the cubic AlNd ($Pm\bar{3}m$) of the CsCl-type with a = 3.74 Å (Stillwell & Jukkola, 1934), and an orthorhombic phase NdAl (*Pbcm*) of the AlDy-type (Buschow, 1965). The 1:2 phase $NdAl_2$ is cubic ($Fd\bar{3}m$), $MgCu_2$-type, with a = 7.86 Å (see Fig. 17), while the 2:1 phase Nd_2Al (*Pnma*) is of the Co_2Si-type (Buschow & Goot, 1971), a structure type very close to the $PbCl_2$-type cotunnite structure. The 1:2 phase has also been obtained with the Ni_2In-type structure in the related compounds Sc_2Al (Eymond & Parthé, 1985) and Nd_2In (Palenzona, 1968; Bazela & Szytuła, 1988).

Two important features should be remarked: the first is that the Ni_2In structure is a superstructure of the AlB_2-type, whose hexagonal c axis is doubled with respect to the AlB_2-type cell. The reason for that will be discussed below. The second is that the related 1:2 compounds $EuGa_2$ (Sichevych & Cardoso-Gil, 2006) and $DyAl_xGa_{2-x}$ ($x \leq 1.2$; Doukoure *et al.*, 1986) are AlB_2-type and hence are intimately related to the 2:1 phases. The existence of $DyAl_xGa_{2-x}$ is relevant because of its high Al content and also because it is isostructural to $SrGa_2$ (Iandelli, 1955). Even the binary $SrAl_2$ compound has not been obtained as AlB_2-type so far; its ambient pressure structure ($CeCu_2$-type) transforms at high pressures into the $MgCu_2$-type (Cordier *et al.*, 1982). This fact, together with the existence of the double $Co_2Si \rightarrow Ni_2In \rightarrow MgCu_2$ transition (Vegas, 2011), leads us to conclude that a continuous solution

between both 1:2 and 2:1 phases might well occur and that an open path seems to exist to transform both the Ni_2In- and AlB_2-type structures into the $MgCu_2$-type, within the Nd–Al system.

5.2. The oxides

Three phases have been reported for the oxides, *i.e.* the $AlNdO_3$ perovskite and the β-aluminas, with compositions $Al_{10.139}Nd_{0.542}O_{16.116}$ ($R\bar{3}m$; Carrillo-Cabrera *et al.*, 1988) and $NdAl_{11}O_{18}$ ($P6_3/mmc$; Iyi *et al.*, 1984). In $Al_{10.139}Nd_{0.542}O_{16.116}$, with the exception of one of the O atoms, all the atomic sites have occupancy factors (*s.o.f.*) less than 1.0.

The underlying idea is that there must be some structural coincidences between the cation sublattices in both phases of the eutectic (the perovskite-like $NdAlO_3$ and the β-alumina-like $NdAl_{11}O_{18}$), on the one hand, and between those phases and the α-Al_2O_3 forming the faceted zones and the substrate, on the other. Next, the cation subarrays of all the oxides involved in the eutectic will be analyzed keeping in mind the structures of the alloys described above. Our aim is to detect the necessary similarities that can justify welding of the eutectic phases at the atomic level.

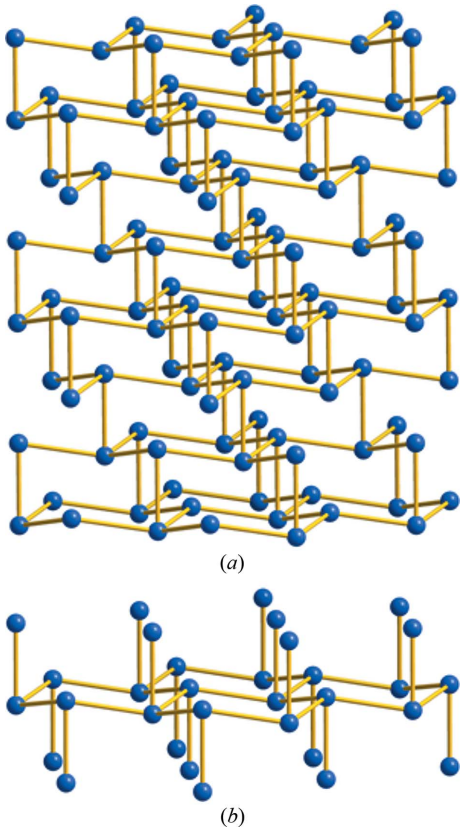

Figure 18
(*a*) The skeleton of Al atoms in corundum showing its fourfold connectivity and its similarity with the structure of Si. (*b*) An isolated fragment of the Al-skeleton showing one of the chair-conformed layers and its fourfold connectivity.

5.3. Description of the involved structures

The first structures to be considered will be those of the substrate, *i.e.* α-, β- and γ-Al_2O_3. In the α-phase (corundum) the Al-sublattice has been described (Ramos-Gallardo & Vegas, 1995) as a three-dimensional structure of four-connected Al atoms, which form chair-conformed layers perpendicular to the *c* axis. This sublattice can be regarded as a variant of the diamond structure (see Fig. 18*a*). They differ, however, in that in Al_2O_3 the interlayer connection occurs through inverted umbrella-like tetrahedra, instead of the regular tetrahedra of the Si-structure. Both features are visible in Fig. 18(*b*). The Al—Al distances in the puckered layers are of 2.78 Å (2.86 Å in f.c.c.-Al).

The phase known as β-alumina really corresponds to a ternary compound of the formula $NaAl_{11}O_{17}$, whose structure is represented in Fig. 19(*a*). Its Al-subarray (blue spheres) can be thought of as being formed by blocks of the hexagonal Fiauf–Laves phases ($MgZn_2$-type) represented in Fig. 20(*a*) (Ramos-Gallardo & Vegas, 1995). These blocks contain frag-

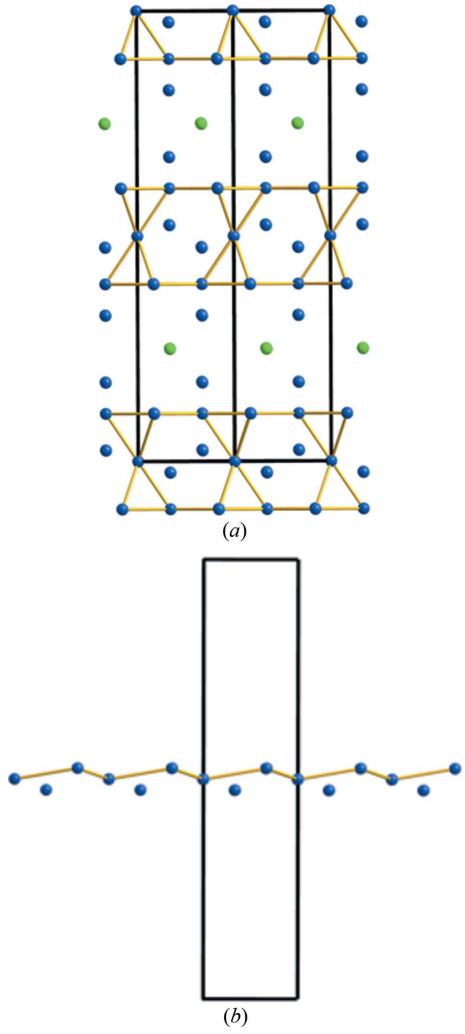

Figure 19
(*a*) The hexagonal structure of $NaAl_{11}O_{17}$ projected on (110). Al: blue; Na: green; the O atoms are omitted. The Al atoms at the central part of the figure are forming the puckered hexagonal layers like that isolated in (*b*).

ments of the spinel-type structure that are highlighted in Fig. 19(*a*), by means of yellow lines connecting the Al atoms (*cf.* Fig. 20*a*). Note that these spinel blocks contain the bulky Al_{12} truncated tetrahedra that are centered by additional Al atoms. The latter, together with the Al atoms located at $z = \frac{1}{2}$, form a diamond-like layer that is represented in Fig. 19(*b*). Note that such layers are topologically similar to those of the corundum structure of Fig. 18(*b*), although in this case the Al–Al distances are elongated to 3.20 Å.

As seen in Fig. 19(*a*), the spinel blocks are intercalated with other moieties of the AlB_2-type. These parts consist of two $\mathbf{3^6}$ planar nets of Al atoms with an intercalated $\mathbf{6^3}$ graphene-like layer of Na atoms (green spheres in Fig. 19*a*). It is noteworthy that this structure is similar to that of the $NdAl_{11}O_{19}$ hexaaluminate, forming part of the eutectic as represented in Fig. 20(*b*). Note also the similarity between the spinel blocks of $NdAl_{11}O_{19}$ and the $MgZn_2$ structure drawn in Figs. 20(*a*) and (*b*).

In the upper part of Fig. 20(*b*), two spinel blocks and one intercalated AlB_2-type block have been highlighted. In Figs. 20(*c*) and (*d*) we have selected the central Al layers of Fig. 20(*b*) that, as in Fig. 19(*b*), are forming a chair-conformed layer projected on the *ab* plane in Fig. 20(*d*). The Al—Al distances within the chairs are also here $\simeq$ 3.20 Å.

Finally, the γ-phase is a defect spinel structure that can be formulated as $Al_{2.8}O_4$. Consequently, its cation array is of the $MgCu_2$-type (cubic Friauf–Laves phases; see Fig. 17). It should be emphasized that in both the β- and γ-Al_2O_3 phases, as well as in the Friauf–Laves phases, the main structural piece is the Al_{12} (Cu_{12}/Zn_{12}) truncated tetrahedron that is centered by Al atoms in alumina and by Mg atoms in both $MgCu_2$ and $MgZn_2$. One isolated $NdAl_{12}$ truncated tetrahedron is represented in Fig. 21(*a*).

It is important to remark that the truncated tetrahedra can be filled not only by Al atoms, but also by some Nd atoms. The latter could facilitate the transition from the corundum structure to both the β- or γ-Al_2O_3 phases, and may also induce the formation of the $NdAlO_3$ perovskite. The transformation corundum $\rightarrow$ γ-Al_2O_3 has also been reported upon high-temperature reduction with small amounts of alkali metals (Dan'ko *et al.*, 2008).

5.4. The eutectic components

In this section we will describe in detail the structures of the phases involved in the eutectic, emphasizing the structural similarities between them.

5.4.1. The hexaaluminate $NdAl_{11}O_{19}$. $NdAl_{11}O_{18}$ exhibits a hexagonal structure of the β-Al_2O_3-type (Iyi *et al.*, 1984; Mizuno *et al.*, 1977). It was described briefly above when compared with the $MgZn_2$ structure (see Fig. 20*b*). The structure of $NdAl_{11}O_{18}$ is an intergrowth of both spinel-type and the AlB_2-type blocks. As mentioned already for the spinel fragments, part of the Al atoms form chair-conformed layers similar to those occurring in α-Al_2O_3 (*cf.* Fig. 19*b* and Fig. 20*c*). The same layer is viewed along the *c* axis in Fig. 20(*d*).

The second block is of the AlB_2-type and is drawn in Fig. 21(*b*), projected on the *ab* plane. This structure is normally

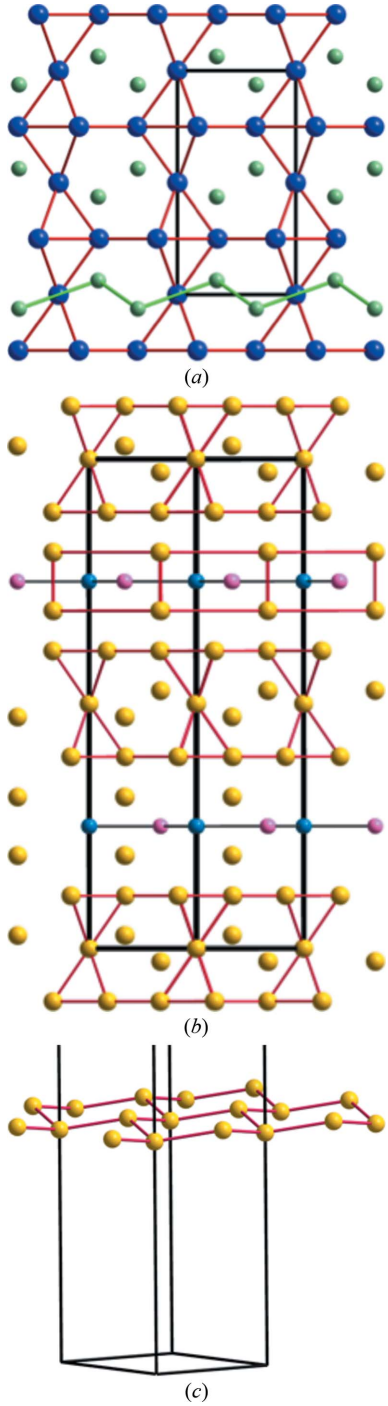

Figure 20
(*a*) The hexagonal structure of the Friauf–Laves phase $MgZn_2$ projected on the *ac* plane. The Zn atoms (blue spheres) form a three-dimensional skeleton of Zn_4 tetrahedra that leave the big Zn_{12} truncated tetrahedra centered by the Mg atoms (green spheres). In the lower part, the Mg atoms are linked to outline the puckered diamond-like layer. (*b*) The hexagonal structure of the $NdAl_{11}O_{19}$ hexaaluminate, similar to that of the β-alumina drawn in Fig. 16(*a*). Al: yellow; Nd: blue/pink; O atoms are omitted. (*c*) The puckered Al-layer formed by the two central Al-sheets in β-alumina. (*d*) The same layer projected on the *ab* plane. Compare with the layers represented in Fig. 16(*b*) and those in corundum in Fig. 15(*b*).

described as the intergrowth of 3^6 planar nets (Al atoms) and graphene-like 6^3 layers (B atoms; Fig. 21*b*). It should be recalled, however, that the structure of Fig. 21(*b*) also represents one half of the unit cell (*c*/2) of a Ni_2In-type structure. This interpretation is highlighted in Fig. 21(*c*), in which the central graphene-like layer is formed by both the Al5 (at 4*e*; *s.o.f* = 0.41) and by the Nd1 atoms (at 2*d*; *s.o.f* = 0.5) so that the layer contains two Al atoms and one Nd atom yielding the stoichiometry $Al3_2[Nd1Al5_2]$. The Al3 atoms forming the 3^6 nets are at 4*f* (*s.o.f.* = 1.0). Both Al6 and Nd2 atoms have been omitted in the picture, while the Al3 atom has been located at the ideal $z = \frac{1}{4}$ position.

Within the 3^6 Al-nets, the Al—Al distances are 5.33 Å and the Nd—Al (Al—Al) distances are close to 3.27 Å. An isolated truncated tetrahedron, like those forming the spinel blocks, is represented in Fig. 21(*a*). Layers denoted as **A** are **3·6·3·6** planar nets (Kagomé nets), whereas the layer denoted as **B** is a 3^6 planar net similar to those forming the AlB_2 fragments of Fig. 21(*b*). The similarity is not only in topology, but also in dimensions, because the Al—Al distances in the **B** layer are also of 5.30 Å.

This coincidence is relevant because it provides an explanation for the intergrowth of both blocks in $NdAl_{11}O_{18}$, a feature that is also supported by the structural transitions $AlB_2 \rightarrow CeCu_2 \rightarrow MgCu_2$ described above for both $SrGa_2$ (Iandelli, 1955) and $SrAl_2$ (Cordier *et al.*, 1982) on one hand, and by the $Ni_2In \rightarrow MgCu_2$ transition occurring in the olivine → spinel transition, on the other hand (Vegas, 2011).

5.4.2. The $NdAlO_3$ perovskite. The second component of the eutectic is the $NdAlO_3$ perovskite. Its structure is a slight rhombohedral distortion [$R\bar{3}c$; a = 3.77 (1) Å; α = 89.63 (2)°] of

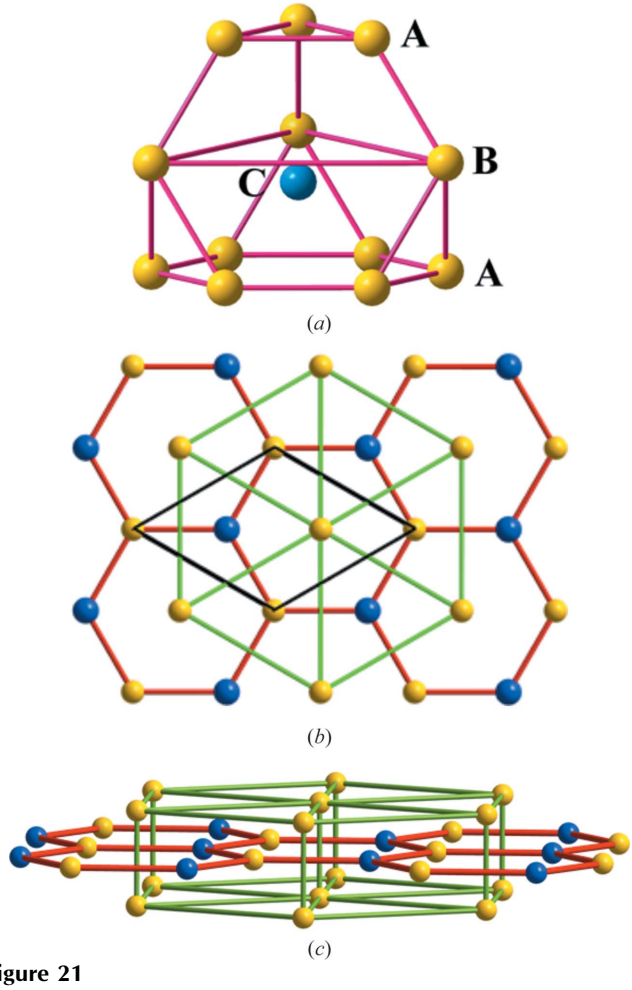

Figure 21
(*a*) Perspective view of an isolated $NdAl_{12}$ truncated tetrahedron. (*b*) The structure of the AlB_2-type (Ni_2In-type) blocks in $NdAl_{11}O_{18}$. Both Al and Nd atoms form 6^3 graphene-like layers alternating with 3^6 planar nets of Al atoms. In agreement with the *s.o.f.* (Iyi *et al.*, 1984), the stoichiometry of the block should be $Al_2(NdAl_2)$, with vacancies in the graphene-like layer. Al: yellow; Nd: blue. In the case of a Ni_2In-type array, yellow and blue spheres correspond to atoms of different species, for example: Ni and In. (*c*) Perspective view of the AlB_2- or Ni_2In-type block. The 3^6 Al-nets are marked with green lines. The graphene-like layers of Al and Nd are drawn with red lines.

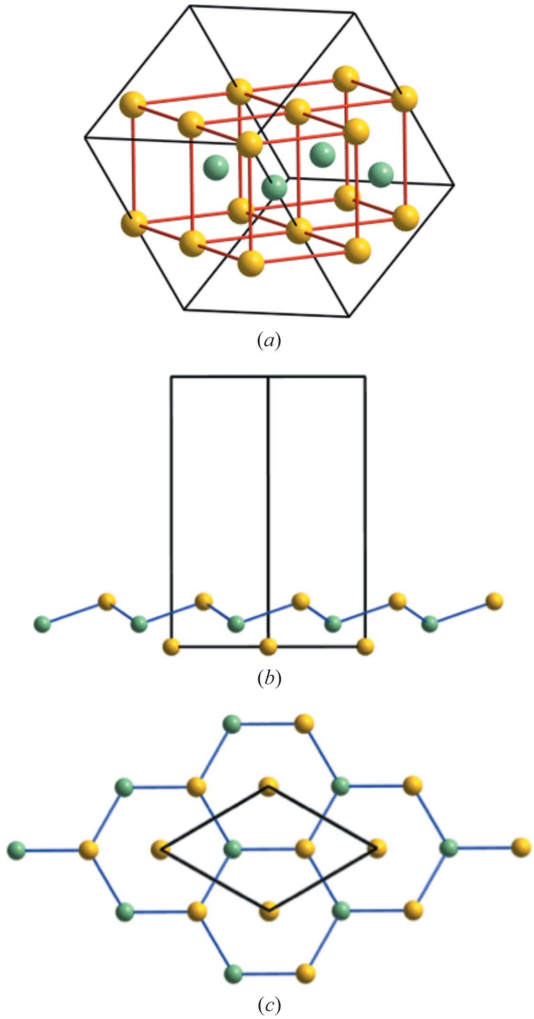

Figure 22
(*a*) The NdAl (CsCl-type) substructure in the rhombohedral perovskite $NdAlO_3$ ($R\bar{3}c$). (*b*) A layer of flattened octahedra ($NdAl_6$) that is part of the $NdAl_8$ cubes. They are projected on the (110) plane of the hexagonal cell. (*c*) The partial structure of (*b*) projected on the *ab* plane. The upper layer of (*b*) shows the Al and Nd atoms connected to form a puckered diamond-like hexagonal net. The lower 3^6 planar net is formed by aluminium atoms. Note its similarity with the partial structure of the AlB_2-type block represented in Figs. 17(*b*) and 18. Al: yellow; Nd: blue–grey.

the ideal cubic structure ($Pm\bar{3}m$) that is stabilized at high temperatures. Its CsCl-type cation array is represented in perspective in Fig. 22(*a*). When the structure is projected on the (110) plane, one can observe the flattened octahedra that constitute the central part of the Al_8 cubes. One layer of such octahedra is represented in Fig. 22(*b*), in which a chair-conformed layer of Nd–Al atoms has been highlighted. The same layer appears projected on the *ab* plane in Fig. 22(*c*).

Surprisingly, this layer is similar in topology and dimensions to that formed by the fragment of the AlB_2-type in the $NdAl_{11}O_{18}$ phase that was represented in Fig. 21(*b*). Moreover, if in Fig. 21(*b*) the Al atoms forming the $\mathbf{3^6}$ planar net are connected with $\frac{1}{2}$ of the Nd atoms of the graphene-like $\mathbf{6^3}$ net, we would obtain a pattern similar to that of Fig. 22(*b*). This result is also of great significance because it provides a physical basis for the intergrowth of $NdAlO_3$ and $NdAl_{11}O_{18}$ of the eutectic through a common structural motif.

5.5. The $NdAlO_3/AlB_2$ (Ni_2In) structural pair

In addition to the arguments given above and based on Fig. 22, the structural similarity between $NdAlO_3$ and $NdAl_{11}O_{18}$, as well as their topological inter-conversion, will be better understood with the drawings represented in Fig. 23. The reader should pay attention to the fact that the AlB_2-type blocks do not have the $NdAl_2$ stoichiometry as they have the related $LnGa_2$ (Haszko, 1961), $Nd(Al_xGa_{2-x})$ ($x = 0.2$; Martin *et al.*, 1980) and Nd(FeGa) at 773 K (Li *et al.*, 2009). Whilst in $LnGa_2$ the graphene-like layer is formed by the Ga atoms, in $NdAl_{11}O_{18}$, however, such layers are formed by both Al and Nd atoms.

Returning again to the $NdAlO_3$ perovskite, its cation array is equivalent to a CsCl-type cube. However, the cube admits a second description analyzed in Fig. 23(*a*). The Al_8 cube can be decomposed into a flattened octahedron whose two basal triangles are capped by two additional atoms forming two additional tetrahedra with the bases. The flattened octahedron (Fig. 23*a*) is formed by the Al1 and Al2 atoms and the cube is completed with the **C** and **C′** capping atoms.

In Fig. 23(*b*) we have redrawn the structure of $NdAl_{11}O_{18}$ described in Fig. 20(*b*). In this case, some Al—Al bonds have been omitted in the upper part of the figure resulting in the isolation of a new polyhedron that has been drawn separately in Fig. 23(*c*). Making a parallel with the cube description of Fig. 23(*a*), this polyhedron can be regarded as one flattened trigonal prism of Al atoms, labeled as Al1 and Al2, centered by a Nd atom. In this case, the bases of the prism are capped by an Al_3 triangle.

The descriptions of Figs. 23(*a*) and (*c*) are important because they inform us about an ideal mechanism by which the $NaAlO_3$ structure can be converted into an AlB_2-type block and *vice versa*. Thus, if we start from the flattened octahedron (Fig. 20*a*) and make the two $\mathbf{3^6}$ Al-planar nets, formed by both Al1 and Al2 atoms, rotate 30° in the opposite way to each other, then the Al_6 flattened octahedron transforms into the trigonal prism of the AlB_2-type drawn in Fig. 23(*c*). In addition, the $NdAl_{12}$ polyhedron of Fig. 23(*c*) also presents similarities with the trun-

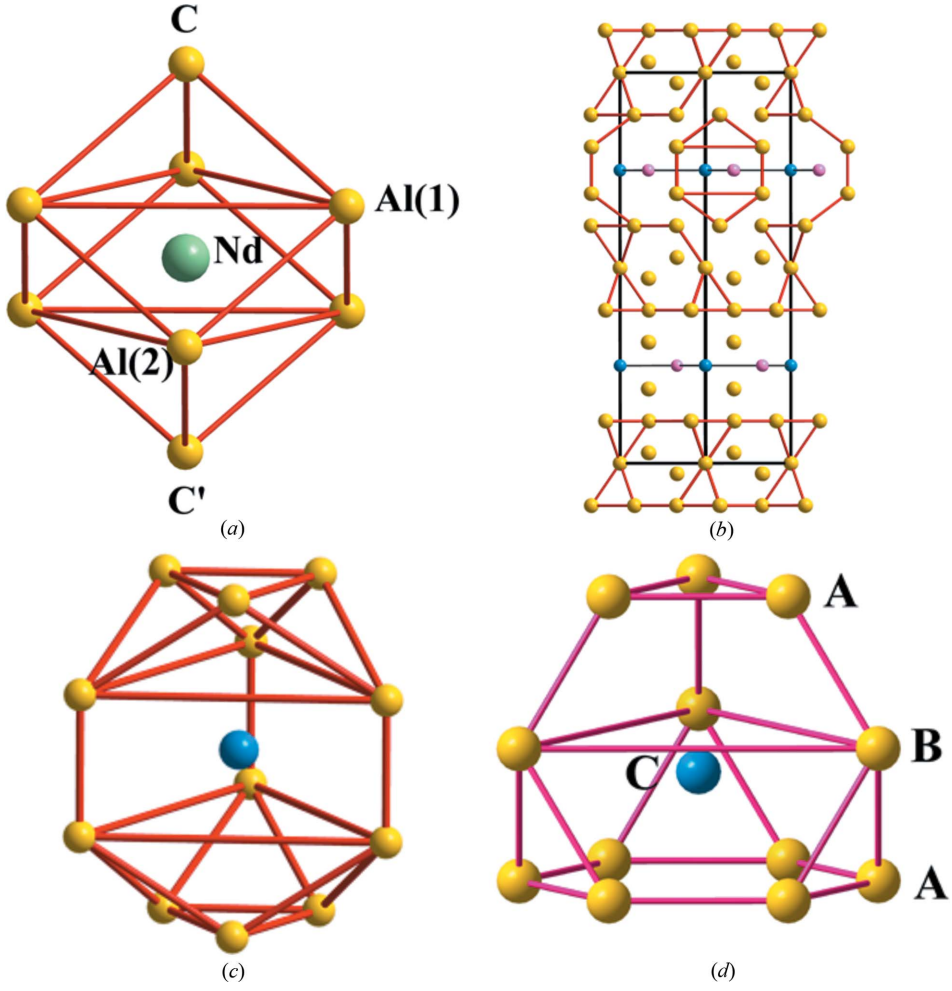

Figure 23
(*a*) Representation of an $NdAl_8$ cube in the perovskite $NdAlO_3$ ($R\bar{3}c$) as a flattened $NdAl_6$ octahedra whose planar faces are capped by two atoms (C and C′) forming extra tetrahedra. (*b*) The structure of $NdAl_{11}O_{18}$ as represented in Fig. 17(*b*), but where the coordination Al-polyhedron surrounding a Nd atom within the AlB_2-type fragment has been isolated by eliminating the Al–Al contacts. (*c*) Perspective view of the same $NdAl_{12}$ polyhedron showing the central trigonal prism capped by two triangular faces. (*d*) The truncated Al_{12} tetrahedron present in the Friauf–Laves phases like $NdAl_2$, in the spinel-type compounds, and also in the β-alumina structure. The A layers are Kagomé nets and the B layers are 3^6 planar nets of dimensions 5.3–5.5 Å. C denotes the central Nd atom. Nd: blue; Al: yellow.

cated $NdAl_{12}$ tetrahedron of the spinel blocks, represented in Fig. 23(*d*).

Such similarities are evident by comparing Figs. 23(*c*) and (*d*). They coincide in the sequence formed by: (*a*) the upper triangular face [Al—Al distances of 2.86 (1) Å]; (*b*) the larger triangular base [Al—Al distances of 5.30 (1) Å]; (*c*) the central Nd atom. This set of atoms constitutes another common structural motif that would induce the junction of both structures. The motifs of Figs. 23(*c*) and (*d*) differ, however, in the relative orientation of the upper Al_3 triangles (**A** in Fig. 20*d*) with respect to the lower triangular face (**B** in Fig. 23*d*).

Because the small **A** triangles are part of a Kagomé net, the different orientations of such triangles in Figs. 23(*c*) and (*d*) can became coincident by a simple translation of the **A** layers. On the other hand, the transformation between the trigonal prism and the flattened octahedron can be achieved if the two bases of the trigonal prism (Fig. 23*c*) rotate 30° with respect to each other, yielding the flattened octahedron of the perovskite (Fig. 23*d*).

The NdAl cube (Fig. 23*a*) should now be compared with the polyhedron isolated from $NdAl_{11}O_{18}$ (Fig. 23*c*). As already discussed, both polyhedra have the existence of the large triangles [Al—Al 5.30 (1) Å] in common. Recall that they differ in their triangular bases. These are capped by only one Al atom in the cube of $NdAlO_3$, whereas the same faces are capped by Al_3 triangles in $NdAl_{11}O_{18}$, giving rise to a CN of 12 Al atoms around each Nd atom, as shown in Fig. 23(*c*). This feature suggests that both polyhedra can only transform into each other if, in the hexagonal hexaaluminate, the spinel-like blocks are displaced perpendicular to the *c* axis with respect to the AlB_2 blocks.

This could be achieved if the three capping Al atoms in Fig. 23(*c*) would displace up to only one of the Al atoms, forming the triangle located over the center of the triangular bases. It is important to highlight that in both spinel and AlB_2 blocks the Nd atoms are surrounded by 12 Al atoms, a CN that lowers to 8 in the perovskite.

Another important aspect to be remarked is the dimension of the fragments. The edge of the $NdAl_8$ cube is 3.77 (1) Å and the Nd—Al distances are 8×3.26 (1) Å. The horizontal edges of the flattened octahedron are in fact six diagonals of the cube faces and their dimensions are of 5.33 (1) Å ($3.77 \times 2^{1/2} = 5.33$). These values are quite close to the dimensions of the corresponding patterns in $NdAl_{11}O_{18}$. Thus, the Al—Al distances in the $\mathbf{3^6}$ Al-layers represented in Figs. 21, 23(*c*) and (*d*) are of 5.55 (1) Å, and the Nd—Al distances are quite close to those found in the perovskite structure [5.33 (1) Å].

The above description has clearly shown that in the $NdAlO_3/NdAl_{11}O_{18}$ eutectic, partial structures exist that are common to both components. Because the central Nd layer is identical in both patterns, the result is that the lower Al2-layers in Fig. 23(*a*) and the central Nd-layer are the common motif in both eutectic components. Both layers are Al- and Nd-$\mathbf{3^6}$ planar nets.

The common block could also be taken as the three-layer Al–Nd–Al set if we admit the displacements mentioned above. The common block can then be even larger by considering the whole $NdAl_8$ cube, whenever the capping atoms of Fig. 23(*c*) have moved adequately.

It is also important to remark that the two substructures present in $NdAl_{11}O_{18}$ (spinel and Ni_2In- or AlB_2-type) are not fortuitous, because both phases can transform into each other. Thus, the *AlB_2 → Laves-phase transition* has been observed experimentally in $ThAl_2$ under pressure (Godwal *et al.*, 1986), the *Ni_2In → Laves-phase* transition occurs in many compounds (Vegas, 2011) as well as in the olivine → spinel transition, and finally that the *(Laves phases) → disordered b.c.c.* transition also occurs in $NbCr_2$ (Mayer *et al.*, 2003). In addition, the NdAl alloy has also been synthesized as a CsCl-type structure. This fact adds a new structural coincidence in the sense that both alloy and oxide maintain topology and dimensions of the NdAl array, as it was earlier reported (Ramos-Gallardo & Vegas, 1997). These structural coincidences indicate that the conversions between partial phases (or fragments) of the eutectic are plausible.

In any case, the common structural fragments (Fig. 23*a* and *c*), and their similar dimensions as well, can serve to assert the possibility of the growth of a phase from the other in the eutectic formation. In other words, such blocks could act as a real *welding interface*, at the atomic level, between the two phases of the eutectic.

6. Conclusions

In previous work (de Francisco *et al.*, 2011) a novel approach towards furthering our understanding of eutectic formation has been proposed. The model contemplates the cation sublattices of the phases involved in the eutectic as responsible for eutectic component coupling at the atomic level. In the present work, this innovative point of view has been applied to the $NdAlO_3/NdAl_{11}O_{18}$ eutectic mixture, in order to test its validity with the measurement of a physical parameter. The identical elastoplastic behavior found in the nanoindentation measurements presented for both components of the eutectic suggests an unequivocal structural continuity within their cation sublattices.

Moreover, according to the concept developed by Vegas and co-workers, the alloy structures are preserved in their corresponding oxides and this outcome provides a rational explanation for the structural relationships observed among the above eutectic phases. Thus, both coating and the eutectic formation need some structural coincidences between the cation sublattices in both phases of the eutectic (the perovskite and the β-alumina-like $NdAl_{11}O_{18}$), on the one hand, and also between those and the α-Al_2O_3 forming the faceted zones and the substrate.

In the case of the perovskite phase, we will apply a similar relationship between the structure of the Friauf–Laves phases $LnAl_2$ (*Ln* = lanthanide), and the metastable b.c.c. structure (disordered CsCl-type) formed by the $LnAl_2$ alloys constituting the $LnAlO_3$ perovskite structure. As mentioned above (de Francisco *et al.*, 2011), such a *Laves phase → b.c.c.* transformation has been reported for the $NbCr_2$ alloy (Mayer

et al., 2003). This transformation of the alloys makes probable that a similar transition can take place in the oxide. In connection with this we must recall the similarities observed in the long '*structural journeys*' of both alloys and oxides (Vegas, 2011). In the case of the Nd–Al system, studied here, we have shown that the $NdAl_2$ subarray converts into the $NdAlO_3$ perovskite structure that contains fragments of the hexagonal structure of β-alumina.

The second component of the eutectic, $NdAl_{11}O_{18}$, exhibits a hexagonal structure of the β-Al_2O_3-type (Iyi *et al.*, 1984; Mizuno *et al.*, 1977). As shown in Figs. 19–23 the similarity of the structural motifs in the α-Al_2O_3-type structure of the faceted zones and with those of the substrate allows the intergrowth of the two eutectic phases and an efficient coupling between them and the substrate. The presence of small intermediate zones of γ-Al_2O_3 between the substrate and the eutectic components should not be discarded. Dan'ko *et al.* (2008) have reported that corundum can transform into γ-Al_2O_3 upon high-temperature reduction with small amounts of alkali metals.

From the figures represented here it can be concluded that both the $NdAlO_3$ perovskite and the β-alumina-type structure of the formula $NdAl_{11}O_{18}$ contain similar fragments that would allow the intergrowth of both structures. In other words, the idea developed in our previous paper (de Francisco *et al.*, 2011) claiming the need for a structural similarity between the cation arrays of the two eutectic components is made evident here and gives support to the experimental observations discussed above.

The set of structures represented above provides a timely insight into how the structures of β-Al_2O_3, the hexagonal Friauf–Laves phase $ZnAl_2$, the $NdAl_{11}O_{18}$ and the perovskite $NdAlO_3$ contain structural elements which can interconvert into each other by small displacements of the atoms. This study provides a new important example that the cation arrays not only govern the structures, but also the eutectics. This means that a degree of continuity within the cation arrays of the components involved is a necessary condition for eutectic formation. In view of the above arguments, it is thus reasonable to propose that cation arrays within the oxide structures may be an essential driving force behind the eutectic formation.

References

Bazela, W. & Szytuła, A. (1988). *J. Less-Common Met.* **138**, 123–128.
Beck, H. P. & Lederer, G. (1993). *Z. Anorg. Allg. Chem.* **619**, 897–900.
Blatov, V. A. & Peskov, M. V. (2006). *Acta Cryst.* B**62**, 457–466.
Blatov, V. A. & Zakutkin, Yu. A. (2002). *Z. Kristallogr.* **217**, 464–473.
Buschow, K. H. J. (1965). *J. Less-Common Met.* **9**, 452–456.
Buschow, K. H. J. & van der Goot, A. S. (1971). *J. Less-Common Met.* **24**, 117–120.
Carrillo-Cabrera, W., Thomas, J. O. & Farrington, G. C. (1988). *Solid State Ionics*, **28–30**, 317–323.
Cordier, G., Czech, E. & Schäfer, H. (1982). *Z. Naturforsch. Teil B*, **37**, 1442–1445.
Coutures, J. P. (1985). *J. Am. Ceram. Soc.* **68**, 105–107.
Dan'ko, A. Ja., Rom, M. A., Sidelnikova, N. S., Nizhankovskiy, S. V., Budnikov, A. T., Grin', L. A. & Kaltaev, Kh. Sh-o. (2008). *Crystallogr. Rep.* **53**, 1112–1118.
Doukoure, M., Gignoux, D. & Sayetat, F. (1986). *Solid State Commun.* **58**, 713–718.
Errandonea, D., Santamaría-Perez, D., Vegas, A., Nuss, J., Jansen, M., Rodríguez-Hernandez, P. & Muñoz, A. (2008). *Phys. Rev. B*, **77**, 094113.
Estepa, C. & de la Fuente, G. F. (2006). Patent 200600560.
Eymond, S. & Parthé, E. (1985). *J. Less-Common Met.* **109**, 345–350.
Francisco, I. de, Lennikov, V. V., Bea, J. A., Vegas, A., Carda, J. B. & de la Fuente, G. F. (2011). *Solid State Sci.* **13**, 1813–1819.
Godwal, B. K., Vijayakumar, V., Sikka, S. K. & Chidambaram, R. (1986). *Physica*, **144**, 44–47.
Haszko, S. E. (1961). *Trans. Met. Soc. AIME*, **221**, 201–202.
Iandelli, A. (1955). *Atti Accad. Naz. Lincei* **19**, 39–43.
Ilyushin, G. D., Blatov, V. A. & Zakutkin, Yu. A. (2004). *Z. Kristallogr.* **219**, 468–478.
Iyi, N., Inoue, Z. & Kimura, S. (1984). *J. Solid State Chem.* **54**, 123–125.
Klimm, D., Ganschow, S., Pajączkowska, A. & Lipińska, L. (2007). *J. Alloys Compd.* **436**, 204–208.
Kokkoros, P. A. & Rentzeperis, P. J. (1958). *Acta Cryst.* **11**, 361–364.
Larrea, A., de la Fuente, G. F., Merino, R. I. & Orera, V. M. (2002). *J. Eur. Ceram. Soc.* **22**, 191–198.
Lennikov, V. V., Pedra, J. M., Gómez, J. J., de la Fuente, G. F. & Carda, J. B. (2007). *Solid State Sci.* **9**, 404–409.
Li, J.-Q., Zhang, W.-H., Yu, Y.-J., Liu, F.-S., Ao, W.-Q. & Yan, J.-L. (2009). *J. Alloys Compd.* **487**, 116–120.
Martin, O. E., Girgis, K. & Niggli, A. (1980). *J. Less-Common Met.* **75**, 151–153.
Martinez-Cruz, L. A., Ramos-Gallardo, A. & Vegas, A. (1994). *J. Solid State Chem.* **110**, 397–398.
Mayer, B., Anton, H., Bott, E., Methfessel, M., Sticht, J., Harris, J. & Schmidt, P. C. (2003). *Intermetallics*, **11**, 23–32.
Mizuno, M., Yamada, T. & Noguchi, T. (1977). *Yogyo Kyokaishi*, **85**, 90–95.
Mora, M., López-Gascón, C., Angurel, L. A. & de la Fuente, G. F. (2004). *Supercond. Sci. Technol.* **17**, 1329–1334.
O'Keeffe, M. & Hyde, B. G. (1985). *Struct. Bond.* **61**, 77–144.
Palenzona, A. (1968). *J. Less-Common Met.* **16**, 379–384.
Ramos-Gallardo, A. & Vegas, A. (1995). *Z. Kristallogr.* **210**, 1–2.
Ramos-Gallardo, A. & Vegas, A. (1996). *Z. Kristallogr.* **211**, 399–403.
Ramos-Gallardo, A. & Vegas, A. (1997). *J. Solid State Chem.* **128**, 69–72.
Santamaría-Pérez, D. & Vegas, A. (2003). *Acta Cryst.* B**59**, 305–323.
Santamaría-Pérez, D., Vegas, A. & Liebau, F. (2005). *Struct. Bond.* **118**, 121–177.
Schön, J. C., Čančarević, Z. & Jansen, M. (2004). *J. Chem. Phys.* **121**, 2289–2304.
Sichevych, O., Cardoso-Gil, R. & Grin', Yu. (2006). *Z. Kristallogr.* **221**, 261–262.
Spiess, M. & Gruehn, R. (1979). *Z. Anorg. Allg. Chem.* **456**, 222–240.
Stillwell, C. W. & Jukkola, E. E. (1934). *J. Am. Chem. Soc.* **56**, 56–57.
Vegas, A. (2000). *Crystallogr. Rev.* **7**, 189–283.
Vegas, A. (2011). *Struct. Bond.* **138**, 133–198.
Vegas, A. & García-Baonza, V. (2007). *Acta Cryst.* B**63**, 339–345.
Vegas, A. & Jansen, M. (2002). *Acta Cryst.* B**58**, 38–51.
Wu, P. & Pelton, A. D. (1992). *J. Alloys Compd.* **179**, 259–287.